Published by IOP Publishing for Sissa Medialab

Received: *November 30, 2019*
Accepted: *January 1, 2020*
Published: *January 28, 2020*

An experimental and GEANT4 simulation study on design of a broad energy-range magnetic spectrograph for laser plasma accelerator

S. Mishra,[a,1] **D. Hazra,**[b] **A. Moorti**[a,b] **and J.A. Chakera**[a,b]

[a] *Laser Plasma Division, Raja Ramanna Centre for Advanced Technology, Indore 452013, India*
[b] *Homi Bhabha National Institute, Training School Complex, Anushakti Nagar, Mumbai 400094, India*

E-mail: shikham@rrcat.gov.in

Abstract: The design and development of a magnetic spectrograph covering a broad electron energy range (few MeV to 1 GeV) for laser plasma accelerators are presented. Two phosphor screens, one in the forward and other in the side direction, were used to record electrons spectra after the dispersion from the magnet. The third phosphor screen was kept in front of the magnet to simultaneously record the electron beam profile. GEANT4 simulations were performed to estimate extra divergence in the electron beam introduced by the phosphor screen kept in front of the magnet. In the magnetic spectrograph setup, the electron beam was transported through a Ti foil of thickness 54 μm from the vacuum chamber, therefore, GEANT4 simulation was performed to estimate the contribution of secondary particles emitted in the front phosphor signal to correctly measure the beam charge. Next, it was used to simulate and design a suitable electron beam dump. Finally, the spectrograph was used to characterize electron beams generated in laser plasma accelerator driven by 120 fs Ti: Sapphire laser pulse and He and Ar gas jet targets.

Keywords: Spectrometers; Models and simulations; Wake-field acceleration (laser-driven, electron-driven)

[1] Corresponding author.

https://doi.org/10.1088/1748-0221/15/01/P01034

Contents

1 Introduction

Advanced acceleration technique based on laser plasma accelerators (LPA) could be a potential alternative over conventional RF based acceleration and therefore has been widely investigated in the last few decades [1, 2]. When high intensity ultrashot laser pulse interacts with underdense plasma, a non-linear plasma wave is generated behind the laser pulse which accelerates plasma electrons, and is known as laser wakefield acceleration (LWFA) mechanism. A major breakthrough in this field was achieved in 2004 [3–5] when three groups simultaneously observed generation of low divergence, narrow energy spread i.e. quasi-monoenergetic electron beams of energy few tens of MeV to few hundreds of MeV, and was subsequently investigated and reported by various other groups worldwide [1, 2, 6, 7]. Generation of quasi-thermal electron beams of several tens of MeV energy has also been observed by Direct Laser Acceleration scheme where electrons oscillating in the plasma channel gains energy directly from the laser field [8–11]. Generation of very high-energy electrons beams has been observed through wakefield mechanism working in the bubble regime [12, 13]. Major achievements towards the generation of GeV class and higher energy electron beams by LWFA mechanism have been achieved using both gas-filled capillary discharge waveguide [14] and gas jet targets [15, 16]. Thus, through LPA electron beams with parameters, viz. beam profile and divergence, energy spectra, and charge, in a wide range are generated [1, 2]. Therefore, the design and development of suitable diagnostics are crucial for the characterization and utilization of electron beams, which in turn also helps in understanding the applicable acceleration mechanisms in LPA [17].

2020 JINST 15 P01034

There are various techniques for energy measurement of electron beams [18, 19]. Electron energy measurement using a magnetic spectrograph has been a conventional but robust technique and widely used for characterization in LPAs [20–23]. In the various magnetic spectrographs designed, laser axis is used to mark the undeflected position of the electron beam on the detector placed after magnet, which in many cases could be misleading due to a mismatch in the electron beam direction from the laser axis and hence can introduce error in the energy measurement of the electron beam. For unambiguous measurement of energy, use of two IPs/Phosphor screens after the magnet was reported and used to correctly estimate the electron beam angle at the exit and entrance of the magnet [24, 25]. However, this technique presents difficulty in use of online mode of operation using phosphor screens. In another design, the use of a phosphor screen before the magnet was suggested to determine the pointing angle of the electron beam with respect to the laser axis, which also helped in the measurement of electron beam profile and divergence [26]. An indirect method of estimation of energy spread of electron beams generated in LPAs, particularly for GeV class energies, was reported using the measurement of undulator radiation [27].

In this paper, design, developent and, use of a magnetic spectrograph for LPA are presented. A C-shaped permanent dipole magnet of field strength ~1 T, and size 10 cms × 20 cms was used to design the spectrograph. Electron beam energy measurement was performed in two configurations i.e. side configuration: 7.5 MeV–80 MeV and forward configuration: 90 MeV–1 GeV. For this, two phosphor screens, one in the forward direction and other in the side direction of C-shaped magnet were used. Hence spectrograph covered a broad energy range of 7.5 MeV–1 GeV. In addition, to record electron beam profile simultaneously, a phosphor screen was also kept in the front of the magnet. This also provided information of electron beam pointing and correlation of electron beam positions on the two phosphor screens which were used to determine the undeflected position of the electron beam for accurate energy measurement. The magnetic spectrograph was used to characterize electron beams generated from the interaction of Ti: Sapphire laser pulses of ~120 fs duration (Intensity ~ 2.2×10^{19} W/cm^2) with an underdense plasma of Ar and He gas-jet targets of 4 mm length, in the density range of 2–30 × 10^{18} cm^{-3} [28].

Next, as transportation of electron beam through phosphor material will introduce the extra divergence in the electron beam, GEANT4 simulations [29, 30] were performed to estimate the divergences for various available phosphor screens and accordingly suitable phosphor was selected to be kept in front of the magnet. Next, the effect of secondary particles on the phosphor signal produced by the interaction of electron beam with a 54 μm thick Ti foil kept in the path for transportation of electron beam from the vacuum chamber to the magnetic spectrograph, which in turn affect the charge measurement, was also estimated. Finally, an electron beam dump was also designed and developed with the optimization of the different thicknesses of the layers for GeV energy electron beams.

2 Design of the magnetic spectrograph

2.1 Magnetic spectrograph: dispersion relations and resolutions

An electron beam passing through magnetic field is dispersed according to its kinetic energy. Electron beam trajectory inside the magnet is described as an arc of the circle as shown in figure 1(a).

2020 JINST 15 P01034

For uniform magnetic field (B), the radius (R) of the relativistic electron trajectory is:

$$R \cong \frac{p}{eB} \cong \frac{E}{ceB} \tag{2.1}$$

Putting all the values in SI units:

$$R\,(m) \cong \frac{E(MeV)}{0.3 \times 10^3 \times B(T)} \tag{2.2}$$

and its trajectory inside the magnet will be given by:

$$x = \sqrt{R^2 - (R - y_m)^2} \tag{2.3}$$

Here x is the distance along the magnet length traveled by the electron beam in the presence of the uniform magnetic field and y_m is the perpendicular distance from the center of the magnet to the edge of the magnet. As shown in figure 1(a), lower energy electron beam will be deflected more and can escape from the side part of the C shaped magnet. On the other hand, higher energy electron beam would propagate through the full length of the magnet and escape from the forward side. Hence, the spectrograph could be used in two configurations depending on the electron beam trajectories: forward configuration where high energy electron beam exiting from the front was detected, and side configuration where lower energy electron beam exiting from the side was detected.

In the side configuration, electron beam exits before traveling the complete magnet length so x changes with respect to the electron beam energies but y_m remains fixed since each electron exiting from side will go through this distance. In forward configuration x becomes equal to the magnet length (L_m) because all high energy electrons travel the complete magnet length but $y_m$changes to y_p and depends on the energy of the electron. If phosphor screens are kept at a distance $D_p$from the magnet in both side and forward configuration then dispersion relation i.e. x_p and y_p with electron energy respectively will be given as:

$$x_p = \frac{D_p\,(R - y_m) + y_m\,(2R - y_m)}{\sqrt{R^2 - (R - y_m)^2}} \tag{2.4}$$

$$y_p = \left(R - \sqrt{R^2 - L_m^2}\right)\left(\frac{D_p L_m}{L_m^2 - R^2 + R\sqrt{R^2 - L_m^2}} + 1\right) \tag{2.5}$$

Electron energy measurement always has some finite energy width which depend on detector resolution as well as on the natural divergence of the electron beam. The energy resolution (r) is termed as $\delta E/E$ or $\delta y/(dx/dE)$ where δy is the width of the detector or natural divergence of the electron beam whichever is higher. Here $(dx/dE)/(dy/dE)$ is the slope of the dispersion curve for side (slope from equation (2.4)) and forward configuration (slope from equation (2.5)) respectively, which is also a function of energy. The resolution for both configurations will be different since

2020 JINST 15 P01034

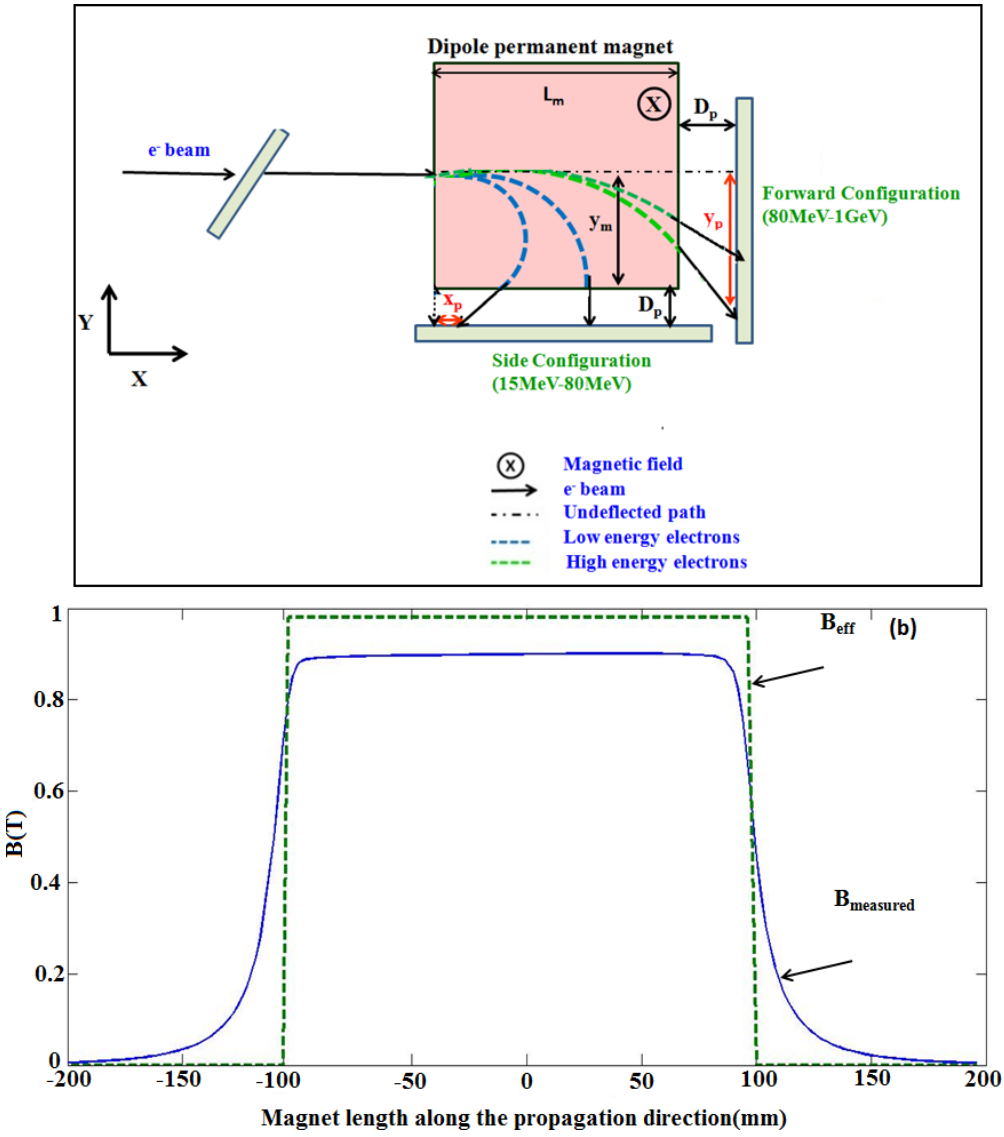

Figure 1. Pictorial representation of electrons trajectories in a rectangular magnetic field for different kinetic energies, higher energy electrons would exit from the forward, lower energy electrons exit from the side of the magnet (b) Magnetic field profile along the length of the dipole magnet (blue curve), and effective magnetic field (green curve).

both have different dispersion curves. So energy resolution for both configurations are:

$$r^{side} = \frac{\delta y}{E}\left(\frac{\left(R^2-(R-y_m)^2\left(\frac{D_pR}{E}+\frac{2y_mR}{E}\right)\right)-\left(D_p\,(R-y_m)+y_m\,(2R-y_m)\right)\frac{y_mR}{E}}{\left(R^2-(R-y_m)^2\right)^{3/2}}\right)^{-1} \tag{2.6}$$

$$r^{front} = \frac{\delta y}{E}\left(\frac{R}{E}\left(1-\frac{R}{\left(R^2-L_m^2\right)^{\frac{1}{2}}}\right)\left(1-\frac{D_pL_mR}{\left(R^2-L_m^2\right)\left(\left(R^2-L_m^2\right)^{\frac{1}{2}}-R\right)}\right)\right)^{-1} \tag{2.7}$$

2020 JINST 15 P01034

In the above equations length (L_m) and width of the magnet (y_m) are fixed and respective values are 20 cm, and 5 cm. Whereas, distnace of phsophors (D_p) from magnet edges for both forward and side configurations could be variable, typical values of 5–10 cm (depending on the desired resolution and imaging set up). Electron beam divergence (δy) could also be varied typically in the range of ~ 5–10 mrad. In the next section 2.3, dispersion curves and resolution values corresponding to the designed spectrograph for LPA are estimated and plotted for typical energy range (15 MeV to 1 GeV). Further, we also estimated the dispersion for given spectrograph parameters using GEANT4 simulation and was found to be matching with the theoretical curve.

In the above treatment edge focusing effect has not been considered. For the forward configuration case, focusing effect in the deflection plane (horizontal plane) would be insignificant (due to close to rectangular magnet configuration), hence, the effect of focusing on the resolution could be ignored. However, there could be a focusing effect on the vertical plane. On the other hand, for electron bending at large angles, and exiting from the side, the effect of focussing in the deflection plane would increase with bending angle and hence affects the resolution at respective energies.

2.2 Dipole magnet

For developing a magnetic spectrograph, a C-type permanent dipole magnet ($B_{eff} \sim 0.98$ T) of dimensions $(20 \times 10 \times 10)\,cm^3$ with pole gap 1.5 cm was used. Magnetic field distribution along magnet length in the magnet pole aperture was measured using tesla meter in both directions from the center of the pole width. Measured magnetic field uniformity in the pole aperture was in good agreement with the design-simulated results. The observed peak magnetic field is 0.9 T with field uniformity 1×10^{-2} over the 80 mm pole width. The effective magnetic (B_{eff}) field has also computed by using the following analytical formula:

$$B_{eff} = \frac{1}{L_m} \int_{-\infty}^{+\infty} B\,(x)\,dx \tag{2.8}$$

Here L_m is the length of the magnet and B(x) is the magnetic field along the direction of the electron beam propagation in the magnet. Magnetic field ($B_{measured}$ and B_{eff}) along magnet length is shown in figure 1(b). The effective magnetic field is estimated to be 0.98 T (using equation (2.8)) which is more than the peak magnetic field and was used in dispersion relations for estimating the energy of the electron beam.

Here one may also consider the temperature effect. The magnet used in the spectrometer is NdFeB (N48 grade) having a maximum operating temperature of 80°C. Whereas, in our case the operating temperature range was 25–30°C. The typical temperature coefficient of $\sim 10^{-3}$/°C for NdFeB (N48 grade) [31] will cause a variation of ~0.1% in the magnetic field, leading to an error of ~0.1% in the electron energy estimation.

2.3 Magnetic spectrograph for laser plasma accelerator (LPA)

Using described magnet a magnetic spectrograph was designed for LPA, as shown in figure 2(a). A high-energy electron beam generated through LPA was transported out of the plasma (vacuum) chamber through a Ti foil of 54 μm thickness placed on the exit port at a distance of ~28 cms from the gas-jet. Two phosphor screens (phosphor-1 and phosphor-2) were used to record electron beam profiles (figure 2(b)), and a correlation between beam positions on them was used for locating

2020 JINST 15 P01034

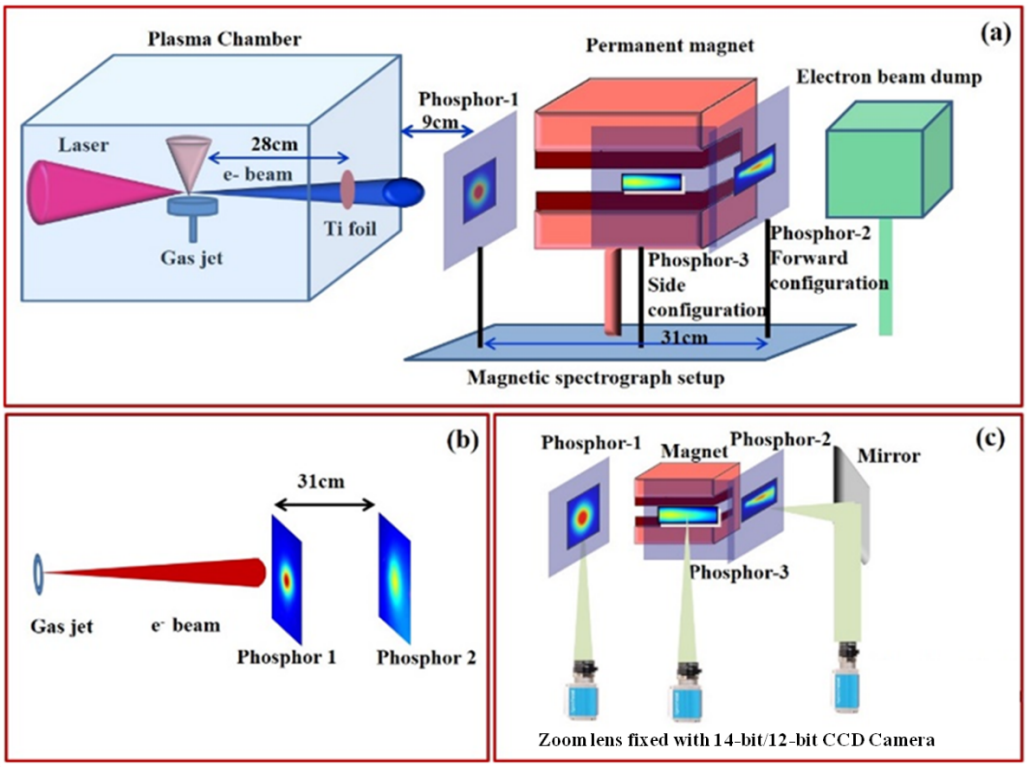

Figure 2. Schematic of the magnetic spectrograph for laser plasma accelerator (LPA). (b) Electron beam profile and position correlation on the two phosphor screens. (c) Imaging set up of the magnetic spectrograph.

undeflected electron beam position on phosphor-2 when a magnet was inserted in between for energy measurement. Dimensions of the phosphor-1 and phosphor-2 were ~8 cm and ~16 cm (diameter) respectively. They were imaged on 14-bit CCD cameras using the Zoom lens covering the full area (figure 2(c)).

All the phosphor screens were covered by 36 μm thick Al foils which blocked the low energy electrons with energy < 70 keV, which was lower than the cut-off energy of < 115 keV for the 54 μm thick Ti foil. Finally, an electron beam dump was used to stop hundreds of MeV to GeV energy electron beams.

To record the electron beam profile simultaneously, a phosphor screen (phosphor-1) was placed before the magnet. The Phosphor-1 was kept at an angle of 45° in the path of the electron beam at a distance of ~9 cms from Ti foil and phosphor emission was imaged directly on a 14-bit CCD camera. For spectrum measurement, in the forward configuration, a phosphor screen (phosphor-2, 20 cm) was kept at a distance of 5 cm from the magnet exit edge. In this case, a 45° folding metal mirror was used to collect the phosphor emission on a 14-bit CCD camera, in order to avoid direct exposure of the CCD to the high-energy electrons. For side configuration of spectrum measurement, another phosphor screen (phosphor-3) was kept towards the magnet side edge at a distance of 7 cm, and was imaged directly on the 14-bit CCD camera.

For the above parameters of the spectrograph, dispersion curves (using equations (2.4) and (2.5)) for side and forward configurations are plotted in figure 3(a) and (b) respectively. The spectrograph

2020 JINST 15 P01034

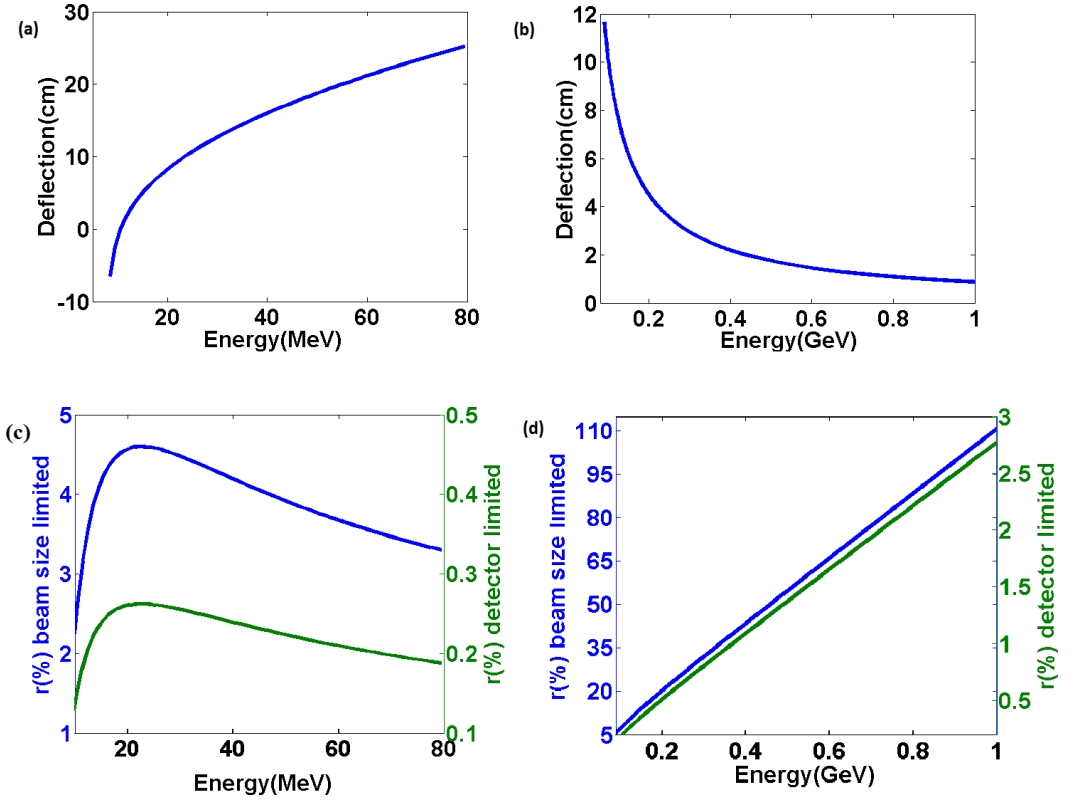

Figure 3. Dispersion curves for (a) side configuration (b) front configuration. Spectrograph resolutions for (c) side configuration (d) front configuration.

covered a broad energy range of 7.5 MeV–1 GeV: side configuration (7.5–80 MeV GeV) and forward configuration (90 MeV–1 GeV). Resolutions are plotted (using equations (2.6) and (2.7)) for both side and forward configuration in figure 3(c) and (d) respectively. In the imaging set up used, 1 pixel (6.45 μm) of CCD camera corresponds to 250 μm (demagnification) on the phosphor screen and therefore limits the resolution of energy measurement. However, the electron beam size itself on the phosphor screen was much larger (~5 mm) and hence the beam natural divergence itself is the limiting factor for the resolution for both the configurations. The resolution was estimated to be <5%, for energy 7.5–80 MeV (side configuration) and was comparatively larger in the forward configuration i.e. ~30% at 300 MeV. Resolution values could be improved further by increasing separation between the magnet exit and the phosphor screen.

Here it may also be important to discuss the effect of error introduced in the electron energy estimation due to accuracy achieved in the measurement of seperation between the edge of the magnet and the phosphor screen (D_p). Due care was taken in the measurement, and a standard steel ruler with 1 mm least count (1% error) was used. This will lead to a corresponding error of (~1%) in the estimation of energy corresponding to a given deflection of the electron beam on the phsophor screen. The associated error would be larger than the error introduced due to CCD pixel size (0.25 mm) for energy estimation below 700 MeV. Therefore, applicability of the detector limited resolution values shown in figure 4d (green curve) has to be seen in this context.

2020 JINST 15 P01034

3 GEANT4 simulations

GEANT4 code was used for simulation of electron beam transport for the present experimental configuration. The simulation parameters used for various investigations (described in the following subsections: 3.1, 3.2 and 3.3) are given in table 1 below.

Table 1. Simulation parameters for all three cases.

Parameters	**Subsection 3.1**		**Subsection 3.2**	**Subsection 3.3**
	Case I	**Case II**		
Divergence (mrad)	Zero	5	5	5
No. of particles	10^6	10^6	10^5	10^5
Energy (MeV)	1–700	150	150	100, 500 and 1000
Energy spread	Mono-energetic	Gaussian (Peak: 150 MeV, Std. Deviation: 30 MeV)	Gaussian (peak 150 MeV, Std. Deviation: 30 MeV)	Mono-energetic

3.1 Selection of phosphor screen and divergence estimation

GEANT4 code was used to estimate the divergence introduced by phosphor-1 placed before the magnet and accordingly appropriate phosphor screen was selected. Three phosphor screens (Gadox:Gd_2O_2S:Tb) viz. Lanex fine, Lanex regular, and DRZ high were considered for simulation (table 2). Although, phosphor screens have thicknesses in hundreds of μm only, still can introduce some divergence in the electron beam due to the high atomic number of the phosphor material.

Table 2. Details of all three phosphors.

Phosphor (different layers)	**Protecting Layer**	**Phosphor Layer**	**Supporting Layer**	**Total Thickness**	**Density (gm/cm^3) (Phosphor layer)**
Lanex Fine	Cellulose acetate (5 μm and 10 μm back and front)	Gd_2O_2S + urethane binder (84 μm)	Poly(ethylene terephtalate) (178 μm)	277 μm	4.25
DRZ-High	PET 9 μm	Gd_2O_2S:Tb + Polyvinyl Butyral binder (310 μm)	Plastic Base 188 μm	507 μm	4.67
Lanex Regular	Not available	Gd_2O_2S:Tb + binder (~200 μm)	Not available	380 μm	~4

2020 JINST 15 P01034

3.1.1 Case I

Estimation of divergences for various phosphor screens was performed considering an electron beam of zero divergences with 10^6 particles. Divergence introduced was estimated for various energies in the range of 1–700 MeV, and is shown in figure 4(a) for different phosphor screens. As expected, divergence value decreased with an electron's energy, and it was found that the Lanex screen introduced less divergence as compared to the DRZ screen. Such an estimation of divergence introduced by phosphor screens using simulations has not been reported earlier. There is an experimental measurement on the divergence introduced by the Lanex fine screen in the similar electron energies range [32] and matches well with the current estimation (less than 2 mrad at energies more than 500 MeV). Based on the above estimation Lanex regular phosphor screen was used to record electron beam profile before magnet (phosphor-1). DRZ high was used to record spectra (phosphor-2 and 3) due to its comparatively higher sensitivity.

3.1.2 Case II

Based on the above investigation, LANEX regular was selected for keeping in front of the magnet. Therefore, further simulation was performed to estimate divergence introduced by this screen for practical electron beams. Simulations were performed for an electron beam with an initial divergence of 5 mrad (typical divergence values obtained in LPA) with a gaussian energy spectrum with a peak energy of 150 MeV and standard deviation of 30 MeV. The input energy spectrum and uniform profile with 5 mrad divergence used are shown in figure 4(b) and (c) respectively. This electron beam was transported from the source through vacuum chamber (medium vacuum: 28 cms), a Ti foil (thickness: 54 μm), air (~9 cms), phosphor-1 (~380 μm thickness and covered by 36 μm thick Al foil), air (~31 cms) to the location of last component i.e. phosphor-2 (figure 2). Electron beam profiles were generated on phosphor-1 and phosphor-2 as shown in figure 4(d) and (e) respectively. Beam divergence estimated on the location of phosphor-1 is ~8 mrad on (figure 4(f)) which is slightly higher than the input beam divergence of 5 mrad. Electron beam size and corresponding divergence estimated at the location of phosphor-2 was found to be much larger to ~29 mrad (figure 4(g)). It may be pointed out here that divergences measured include the effect of all components kept in the electron beam path. Divergence introduced by various components were estimated through simulation considering a parallel beam and found to be 2.5 mrad (54 μm of Ti), 1.11 mrad (air of 9 cms), 1.22 mrad (36 μm of Al foil), 13.15 mrad (Phosphor-1 material) and 2.24 mrad (~31 cms of air).

3.2 Estimation of contribution of secondary particles emissions on phosphor signals

Now we estimate the flux of secondary particles emitted by the interaction of electron beam and Ti foil and its contribution in the measurement of the phosphor-1 signal which was kept close to it at a distance of ~9 cms. In order to get the spectrum of secondary particles GEANT4 simulations were performed for 30 MeV and 150 MeV electron beams transported through 54 μm thick Ti foil and results discussed below are for 150 MeV case and it was similar for 30 MeV in case of secondary electrons (i.e. considerable flux at ~2–3 MeV) [33]. However, in the case of photons, the energy of the photons would be higher. Typical energy spectra for secondary electrons and photons are shown in figure 5(a) and (b) respectively. For input primary electrons of 10^5 considered in simulation, the

2020 JINST 15 P01034

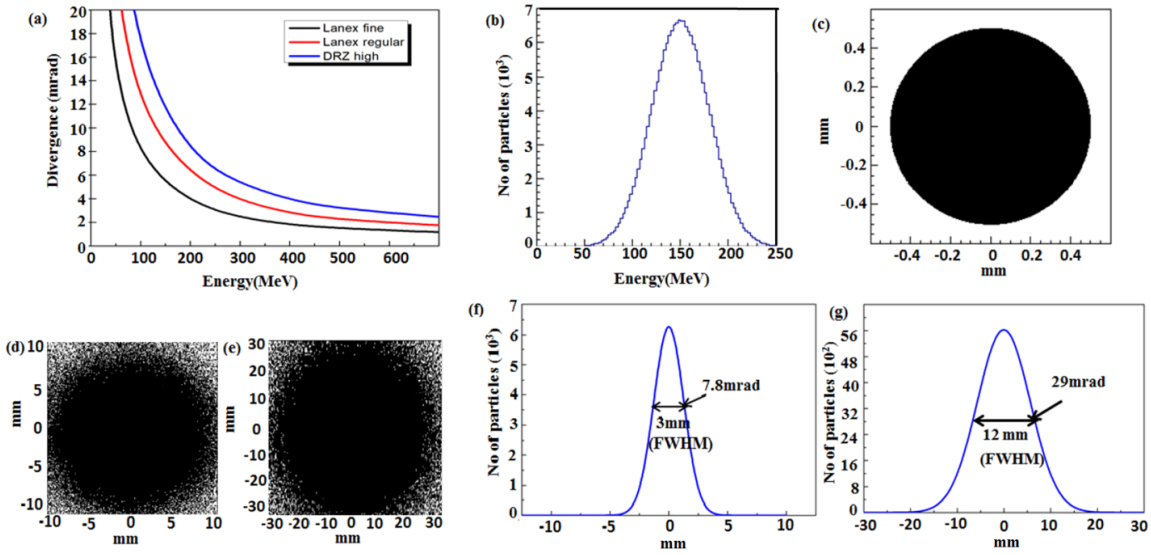

Figure 4. (a) Divergence introduced vs energy of the electron beam for three different phosphors for a collimated beam, (b) Input energy distribution of electrons defined in the GEANT4 simulations (c) Input electron beam profile. Output electron beam profile at (d) Phosphor-1 and (e) Phosphor-2, and corresponding lineouts (f) at Phosphor-1 and (g) at Phosphor-2.

flux of secondary electrons generated was statistically in the range of ~1–2%, with ~90% of flux at ~2–3 MeV and remaining at ~4–10 MeV. Electrons of less than 2 MeV energy, scattered at larger angles to be detected on phosphor-1 position (~9 cm from the Ti foil) and hence, the contribution to phosphor emission could be ignored. The energy deposition curve was generated for Lanex regular phosphor screen (figure 5(c)) using GEANT4 and was found to be similar to the sensitivity curve [34] of DRZ High and Lanex fine phosphor screen reported earlier for incident electron beam at various energies. For energy at ~2–3 MeV, energy deposition is ~1.5X as compared to the constant value of deposition at more than 4 MeV. If we consider the flux and the ratio of energy deposition by the secondary electrons than the contribution in total counts observed on phosphor-1 will be ~2.7% by secondary electrons at ~2–3 MeV and less than 0.1% by the remaining secondary electrons.

Next, the energy range of secondary photons was ~5–140 MeV, with considerable flux in the range of 5–30 MeV. Photons of energy less than ~5 MeV will anyway much more scattered to be detected on phosphor-1. For the 10^5 primary electrons incident on phosphor-1, the flux of photons detected was estimated to be ~4%. The sensitivity curve of phosphor (Gadox) screen for photons [35] has been reported which shows the photons with energy 1 MeV has 0.5% energy absorption within the phosphor material which reduces sharply for higher energy photons of ≥ 5 MeV. Hence the contribution of secondary photons in the counts observed on phosphor-1 would be much less than ~1% and hence is insignificant.

It may be pointed out here that such an estimation of secondary particles is of significance as usually phosphor calibration could also be used to estimate the charge of the electron beams [34, 36]. For accurate charge calibration number, it is necessary to estimate secondary particles contribution in measured phosphor signal and therefore requires correct estimation of the secondary spectrum, energy and corresponding phosphor sensitivity in that range. As per the present estimation described above, it is found that secondary particles will affect the charge estimation by <3% only.

2020 JINST 15 P01034

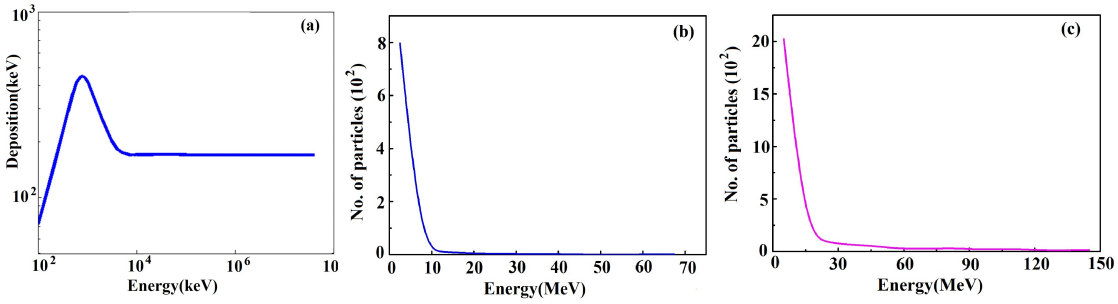

Figure 5. (a) Simulated energy deposition by the collimated electron beam in Lanex Regular phosphor screen (b) Spectrum of secondary e^- generated through Ti foil (c) Spectrum of secondary gamma generated through Ti foil.

3.3 Design of a beam dump

In laser plasma accelerators electrons in the energy range of hundreds of MeV to GeV are generated. High energy electron beam and generated bremsstrahlung after interaction with surrounding materials can damage the electronic devices as well as add to the background noise in the phosphor signal which could decrease the detection sensitivity. Therefore, a suitable dump is required for such high energy electron beams. Accordingly, an electron beam dump was designed using GEANT4 simulations for hundreds of MeV to GeV energy scale and was also set up. As these high energy beams could also generate secondary radiations so shielding of radiations in beam dump design was also included. As the electron beam passes through the thick material it can interact via ionization (secondary electrons), bremsstrahlung radiation, pair production, reflection (backscattering), etc. with the material.

In order to simulate the beam dump in GEANT4, 10^5 number of particles were considered for tracking history through all the layers of the beam dump for three different electron energies of 100 MeV, 500 MeV, and 1 GeV. The geometry and design of the beam dump simulated are shown in figure 6.

The stacking of the different materials in the beam dump was layered based on electron interaction with materials of various atomic number (Z). Probability of production of bremsstrahlung increases by high energy electrons (>100 MeV) interaction with higher Z. Therefore, the first layer of the beam dump was made of Teflon block (lower Z). Ranges of the 100 MeV, 500 MeV and 1 GeV electron beams in Teflon are ~16 cm, ~36 cm and ~47 cm respectively. Based on that Teflon blocks were chosen to be 20 cm so that it could completely stop the 100 MeV energy electron beam and significantly cut the 500 MeV (500 MeV to ~137 MeV) and 1 GeV (1 GeV to ~294 MeV). The next layers were made of relatively higher density metal i.e. Aluminium and Copper respectively (5 cm thick each). The electron beam of 500 MeV and 1 GeV up to the Aluminium layer reduce to ~59 MeV and ~182 MeV which have the ranges of ~2 cm and ~3.5 cm respectively in Copper. Therefore, the Copper block of 5 cm was sufficient to stop electron beam up to 1 GeV (table 3). Next, since the range of 1 GeV electrons is less than the 5 cm Copper but due to range straggling some electrons escape from the Copper layer. Therefore, an extra protection layer of a lead of 5 cm was used after the Copper layer to stop remaining electrons. As can be seen, electrons of 100 MeV, 500 MeV and 1 GeV are stopped by the Teflon (20 cm), (Teflon (20 cm) +Al (5 cm) +Cu

2020 JINST 15 P01034

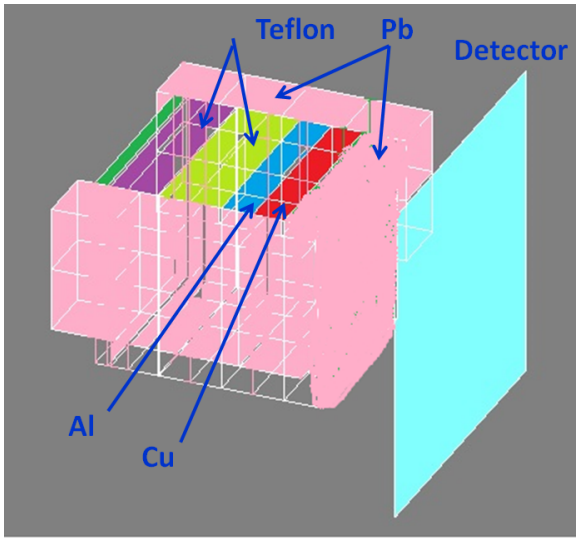

Figure 6. Structure of high-energy electron beam dump.

Table 3. Transmission of the primary electron beam from layers of the beam dump.

Energy (GeV)	Teflon (20 cm)	Al (5 cm)	Cu (5 cm)	Pb (5 cm)
0.1	8%	0.005%	–	–
0.5	49%	28%	0.064%	–
1	66%	48%	2%	<1%

(5 cm) and Teflon (20 cm) +Al (5 cm) +Cu (5 cm)+ lead (5 cm) respectively. At such high energies backscattering of the primary electrons (by Teflon layer) was <1% and hence could be ignored [33].

Stacking of all above mentioned layers stopped the electrons up to GeV energy but the interaction of such high energy electrons produced a large amount of bremsstrahlung and secondary electrons by the interaction with various layers. In principle, 1 GeV electrons could have been stopped using a single layer of 50 cm thick Teflon but this would also lead to the generation of a large flux of bremsstrahlung radiation (tables 4 and 5), for which extra layers of higher-Z materials would be required, leading to the comparatively larger size of the beam dump.

The typical mean energies of the bremsstrahlung and secondary electrons generated by first layer of Teflon of 20 cm thickness were in the range of few MeV to tens of MeV for 100 MeV, 500 MeV and 1 GeV electron beams. Shielding of this radiation was performed by using optimum thickness of the last lead layer. In order to optimize lead thickness for 100 MeV electrons, generated high energy radiation are significantly stopped by the 10 cm thick lead block.

But in the case of 500MeV and 1 GeV, average energy of the secondary bremsstrahlung and electrons are comparatively higher, so a larger thickness of 20 cm lead will be required, as shown in table-IV and V. For such a combination, the mean energy of both bremsstrahlung and secondary electrons were less than 1 MeV after last layer of the beam dump. Hence, with an overall length of 50 cm, all the primary and secondary radiations could be stopped which would not have been

2020 JINST 15 P01034

Table 4. Generation of the secondary gamma from different layers of the beam dump.

Energy (GeV)	(i) Teflon (20 cm)	(ii) Teflon (50 cm)	(iii) (Teflon(20 cm)+ Al(5 cm)	(iv) Teflon(20 cm)+ Al(5 cm)+Cu(5 cm)	(iv) + Pb (5 cm)	(iv) + Pb (10 cm)	(iv) + Pb (15 cm)	(iv) + Pb (20 cm)
0.1	3.2×10^5	9×10^4	2.4×10^5	1.5×10^5	1.8×10^4	$\mathbf{4.2\times10^3}$	2×10^3	8.7×10^2
0.5	1.03×10^6	1.6×10^6	1.3×10^6	1.8×10^6	$3.\times10^5$	3.8×10^4	7.2×10^3	$\mathbf{2.8\times10^3}$
1	1.35×10^6	2.18×10^6	1.9×10^6	4×10^6	9×10^5	1.1×10^5	1.5×10^4	$\mathbf{4\times10^3}$

Table 5. Generation of the secondary electrons from different layers of the beam dump.

Energy (GeV)	(i) Teflon (20 cm)	(ii) Teflon (50 cm)	(iii) (Teflon(20 cm)+ Al(5 cm)	(iv) Teflon(20 cm)+ Al(5 cm)+Cu(5 cm)	(iv) + Pb (5 cm)	(iv) + Pb (10 cm)	(iv) + Pb (15 cm)	(iv) + Pb (20 cm)
0.1	1×10^4	3×10^3	5×10^3	2.8×10^3	2.9×10^2	**stopped**	–	–
0.5	7.5×10^4	6×10^4	9.2×10^4	5.8×10^4	5.1×10^3	6×10^2	1.9×10^2	**stopped**
1	1.21×10^5	1.48×10^5	1.84×10^5	1.55×10^5	1.6×10^4	1.7×10^3	3×10^2	**stopped**

possible with a single layer of low-Z Teflon material of 50 cm thickness as pointed out above also. The transverse dimension of various blocks used in beam dump was 30×30 cms to cover large divergence and also energy dispersed electron beams. For extra protection, stacking of a layer of 5 cm thick lead blocks was also used in the side directions. Primary electrons and secondary radiation (both electrons and photons) in the side directions of the beam dump were less than 1% for 100 MeV to 1 GeV electron energy.

4 Calibration of the magnetic spectrograph

Magnetic spectrograph is a standard established technique for high-energy electron beam energy measurement and particularly widely used for investigations performed on laser plasma accelerators [15–20]. In LPA investigations, mostly laser axis is considered as the undeflected position of the electron beam on the phosphor screen. However, electron beam may have some angle with respect to the laser axis and also pointing variation, which would lead to the error in energy estimation. There are several reports of magnetic spectrograph design [24–26] for removing this ambiguity. We have used a correlation relation between two phosphors kept in the electron beam path for estimating the undeflected position of the electron beam on the phosphor-2 (as described in section 2.3). For each position of electron beam observed at phosphor-1 corresponding positions on the phosphor-2 were recorded. This was used for marking the undeflected position of the electron beam on the phosphor-2 when the magnet was inserted after phosphor-1 for energy measurement. It may be mentioned here that, the electron beam position variation (pointing stability) along the magnet dispersion axis on the phosphor-1 was within 5 mrad with respect to the mean position, and the corresponding variation on phosphor-2 was within 3 mrad. The above pointing variation would lead to the energy measurement error of ~5% which is less than the resolution of the magnetic spectrograph for forward configuration used for He gas jet targets.

Next, we have derived the absolute electron energy spectrum from the recorded energy spectrum. Absolute electron beam spectrum (dN_{el}/dE) (where N_{el} is the number of electrons), is given

2020 JINST 15 P01034

by the following relation [20]:

$$\frac{dN_{el}}{dE}(E_o) = \frac{\text{Counts}\,(E_o)}{\text{pixel size}} \times \frac{ds}{dE} \div \frac{dN_{counts}}{dN_{coll}} \times \frac{dN_{coll}}{dN_{cr}} \frac{dN_{cr}}{dN_{el}}$$

Here, Counts (E_o) = counts in the CCD per pixel at given energy E_0, pixel size = size of the pixel along Phosphor-2 screen (250 µm in our experimental conditions). ds/dE = derivative of the dispersion relation at E_0, where s is the deflection from the undeflected position.

The first term in denominator is the CCD yield given as:

$$\frac{dN_{counts}}{dN_{coll}} = \frac{QE}{r}$$

Conversion of collected photons into CCD counts, where QE is the quantum efficiency of the CCD (62% for 14-bit and 12-bit pixelfly CCD camera at 546 nm) and r is the read out factor i.e. CCD electron/count (1.5 for 14-bit and 3.8 for 12-bit CCD).

The second term in the denominator is collection efficiency of the system which depends on the solid angle (Ω) of collection and transmission factors of imaging optics:

$$\frac{dN_{coll}}{dN_{cr}} = \Omega \times \text{lens transmission} \times \text{Filter factor}$$

The last term (dN_{cr}/dN_{el}) in the denominator is the conversion efficiency of the phosphor screen from number of electrons to photons. The phosphor screens used for electron beam profile and energy spectrum were well calibrated screen [34, 36] and same were used here.

5 Use of magnetic spectrograph in LPA

Magnetic spectrograph designed and developed was used for characterization of high-energy electron beams for experimental investigation on LPA (figure 6) in single shot mode as per set up shown in figure 2(a).

A gas-jet target using a slit nozzle of size 1.2 mm × 4 mm was set up inside a vacuum chamber. Gases used were He and Ar, and gas density in the gas-jet was varied by changing backing pressure, which was typically used in the range of 1–5 bar.A laser beam (150 TW Ti: Sapphire laser) was focused along 4 mm length using a 50 cm focal length Off Axis Parabola (OAP) to a focal spot of ~8 µm FWHM (Full width at half maximum). Considering ~23% energy inside it, intensity of $\sim 2.2 \times 10^{19}$ W/cm^2 was estimated for laser pulse duration of 120 fs. A schematic of the experimental set up of magnetic spectrograph is shown in figure 7. Electron beam profile and spectrum obtained from both He and Ar gas jets were characterized separately in different energy measurement configuration.

For He gas-jet target, on phosphor-1, electron beam size was found to be ~3–5 mm (FWHM) and which increased to ~10–15 mm (FWHM) on phosphor-2 kept at a distance of 31 cm from the phosphor-1. Divergence at phosphor-1 and after exiting is calculated to be ~ 9 mrad and ~32 mrad respectively, which is close to the values obtained through simulation also (figure 4(e) and (f)). A typical electron beam profile (recorded on phosphor-1) and its corresponding raw spectrum recorded on forward phosphor screen (phosphor-2) for He gas-jet target are shown in figures 8(a) and 8(b) respectively. Absolute spectrum (dN/dE) is also plotted in figure 8(c). The electron beam was

2020 JINST 15 P01034

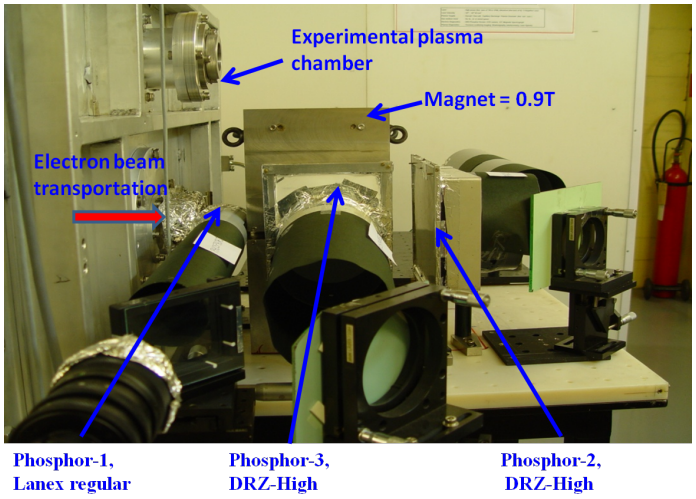

Figure 7. Picture of developed magnetic spectrograph set up used in laser plasma accelerator (LPA).

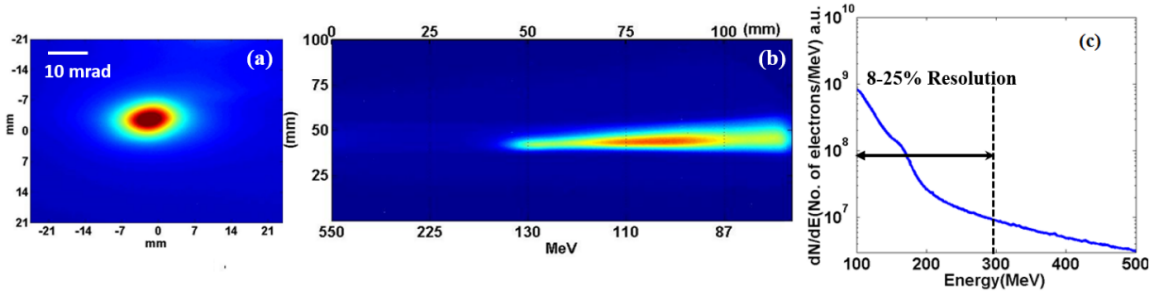

Figure 8. Characterization of LPA electron beams generated using He gas-jet target, (a) Electron beam profile recorded on Phosphor-1 (b) Electron beam spectrum recorded on Phosphor-2, (c) Absolute spectrum. Corresponding resolution values from figure 3(d) is also shwon.

found to be well collimated as shown in profile recorded on phosphor-1 as shown in figure 8(a). Electron beam energy recorded showed energy >84 MeV and extending to beyond >300 MeV with a resolution of 8–25%. It may be pointed out here that no spectrum was observed on phosphor-3 (side phosphor) that shows only high energy electrons (more than 80 MeV) were generated.

In the case of Argon gas-jet target low energy electrons spectrum was observed on the side screen (side configuration). However, no spectrum was observed on phosphor 2. It shows that with Ar only low energy electron beams are generated. Hence, no phosphor correlation was required for this configuration. Typical electron beam profile (recorded on phosphor-1) and its corresponding spectrum (recorded on phosphor-3) for Ar gas-jet target are shown in figure 9(a) and 9(b) respectively. Absolute spectrum (dN/dE) is also plotted in figure 9(c). Electron beam profile was scattered and it covered all area of phosphor-1 (diameter ~7 cms). Electrons energy range was of the order of ~14 MeV to 60 MeV with a resolution of 2–5%. Hence, the sensitivity of the magnetic spectrograph was found well even at very low energies covering a broad energy range. Acceleration mechanisms of electrons are attributed to the DLA and wakefield mechanisms in case of Ar and He gas-jet targets respectively and can be a subject of another paper.

2020 JINST 15 P01034

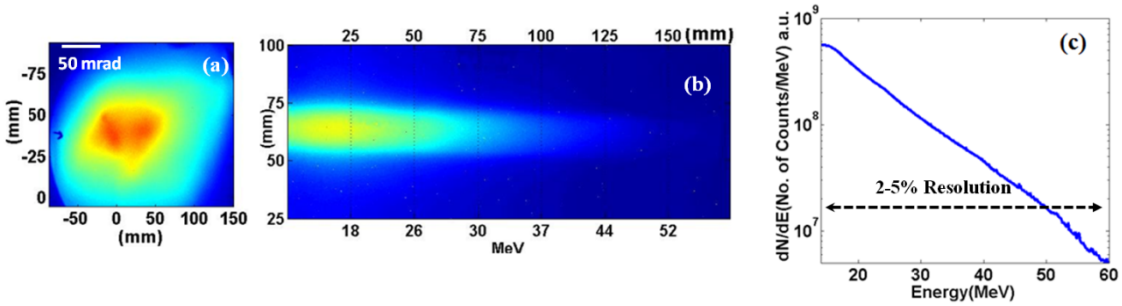

Figure 9. Characterization of LPA electron beams generated using Ar gas-jet target, (a) Electron beam profile recorded on Phosphor-1 (b) Electron beam spectrum recorded on Phosphor-3, (c) Absolute spectrum. Corresponding resolution values from figure 3(c) is also shwon.

6 Conclusion

A magnetic spectrograph for simultaneous recording and measurement of high energy electron beam profile and its spectra covering a broad range of electrons energy (~0.075–1 GeV) using both side and forward configurations, was designed and developed. It was used to characterize high-energy electron beams generated in laser plasma accelerator (LPA) and electron beams of energy ~84–500 MeV (He gas jet) and ~14–60 MeV (Ar gas jet) were recorded in forward and side configurations respectively. Further, GEANT4 simulations for our experimental parameters and conditions were performed. First, it was performed to estimate divergence introduced by various phosphor screens and shows divergence <2 mrad for a collimated beam at energies more than 500 MeV for the Lanex regular and the Lanex Fine phosphor screen. Simulations were also performed for practical electron beams by taking initial finite divergence (5 mrad) and were found that divergence becomes ~7 mrad and ~29 mrad on Lanex Regular and DRZ-high respectively which gives good agreement with the experimental results of ~8 mrad and ~26 mrad respectively. Next, simulations were also performed for estimating the contribution of secondary electrons and photons emitted by the interaction of electron beam with 54 μm thick Ti foil kept in the electron beam path in phosphor signal. Contribution was found to be mainly due to secondary electrons generated which was also estimated to be <3% only. Finally, an electron beam dump was designed and set up with an optimized size of 50 cm (thickness along beam propagation) and $30 \times 30\,\text{cm}^2$ (transverse). Dimensions of the beam dump were kept such that it could cut the significant primary energy as well as could produce minimum high energy radiations. Therefore it was developed for stopping electron beam from hundreds of MeV to GeV scale of energies.

Acknowledgments

We acknowledge the support provided by R.A. Khan, and A. Singla for the laser operation, D. Karmakar for help in setting up the experiment, R.K. Bhat for computer and electronics support, and R.P. Kushwaha, S. Sebastin, K.C. Parmar and L. Kisku for providing mechanical/workshop support. We also thank Shri R.S. Shinde, AMTD, RRCAT and his team Shri Vinod Gaud, P.K. Kulshreshtha, Prashant Pareek, Karan Singh for providing us C-shaped permanent dipole magnet used for design and development of magnetic spectrograph. One of the authors, SM, expresses her gratitude to Shri Raman Sehgal, BARC, Mumbai, for his guidance and help in learning GEANT4 simulations.

2020 JINST 15 P01034

References

[1] E. Esarey, C.B. Schroeder and W.P. Leemans, *Physics of laser-driven plasma-based electron accelerators*, *Rev. Mod. Phys.* **81** (2009) 1229.

[2] C. Joshi, *Plasma-based accelerators: then and now*, *Plasma Phys. Control. Fusion* **61** (2019) 104001.

[3] S.P.D. Mangles et al., *Monoenergetic beams of relativistic electrons from intense laser-plasma interactions*, *Nature* **431** (2004) 535.

[4] C.G.R. Geddes et al., *High-quality electron beams from a laser wakefield accelerator using plasma-channel guiding*, *Nature* **431** (2004) 538.

[5] J. Faure et al., *A laser-plasma accelerator producing monoenergetic electron beams*, *Nature* **431** (2004) 541.

[6] B.S. Rao, A. Moorti, P.A. Naik and P.D. Gupta, *Effect of chirp on self-modulation and laser wakefield electron acceleration in the regime of quasimonoenergetic electron beam generation*, *Phys. Rev. ST Accel. Beams* **16** (2013) 091301.

[7] B.S. Rao, A. Moorti, R. Rathore, J.A. Chakera, P.A. Naik and P.D. Gupta, *High-quality stable electron beams from laser wakefield acceleration in high density plasma*, *Phys. Rev. ST Accel. Beams* **17** (2014) 011301.

[8] A. Pukhov, Z.M. Sheng and J. Meyer-Ter-Vehn, *Particle acceleration in relativistic laser channels*, *Phys. Plasmas* **6** (1999) 2847.

[9] C. Gahn et al., *Multi-MeV Electron Beam Generation by Direct Laser Acceleration in High-Density Plasma Channels*, *Phys. Rev. Lett.* **83** (1999) 4772.

[10] J.L. Shaw et al., *Role of Direct Laser Acceleration of Electrons in a Laser Wakefield Accelerator with Ionization Injection*, *Phys. Rev. Lett.* **118** (2017) 064801.

[11] D. Hazra, A. Moorti, B.S. Rao, A. Upadhyay, J.A. Chakera and P.A. Naik, *Betatron resonance electron acceleration and generation of relativistic electron beams using 200 fs Ti:sapphire laser pulses*, *Plasma Phys. Control. Fusion* **60** (2018) 085015.

[12] A. Pukhov and J. Meyer-ter-Vehn, *Laser wake field acceleration: the highly non-linear broken-wave regime*, *Appl. Phys.* **B 74** (2002) 355.

[13] W. Lu et al., *Generating multi-GeV electron bunches using single stage laser wakefield acceleration in a 3D nonlinear regime*, *Phys. Rev. ST Accel. Beams* **10** (2007) 061301 [physics/0612227].

[14] A.J. Gonsalves et al., *Petawatt Laser Guiding and Electron Beam Acceleration to 8 GeV in a Laser-Heated Capillary Discharge Waveguide*, *Phys. Rev. Lett.* **122** (2019) 084801.

[15] X. Wang et al., *Quasi-monoenergetic laser-plasma acceleration of electrons to 2 GeV*, *Nat. Commun.* **4** (2013) 1988.

[16] H.T. Kim et al., *Enhancement of electron energy to multi-GeV regime by a dual-stage laser-wakefield accelerator pumped by petawatt laser pulses*, *Phys. Rev. Lett.* **111** (2013) 165002 [arXiv:1307.4159].

[17] M.C. Downer, R. Zgadzaj, A. Debus, U. Schramm and M.C. Kaluza, *Diagnostics for plasma-based electron accelerators*, *Rev. Mod. Phys.* **90** (2018) 035002.

[18] E. Tegeler and G. Ulm, *Determination of the beam energy of an electron storage ring by using calibrated energy dispersive Si(Li) detectors*, *Nucl. Instrum. Meth.* **A 266** (1988) 185.

2020 JINST 15 P01034

[19] A.S. Müller, *Measurements of Beam Energy*, in *Proceedings of CERN Accelerator School (CAS)*, CERN-2009-005, Dourdan, pp. 427–451 (2009).

[20] Y. Glinec et al., *Broadrange Single Shot Electron Spectrometer*, *Rev. Sci. Instrum.* **77** (2006) 103301.

[21] K. Nakamura, W. Wan, N. Ybarrolaza, D. Syversrud, J. Wallig and W.P. Leemans, *Broadband single-shot electron spectrometer for GeV-class laser-plasma-based accelerators*, *Rev. Sci. Instrum.* **79** (2008) 053301.

[22] C.M.S. Sears et al., *A high resolution, broad energy acceptance spectrometer for laser wakefield acceleration experiments*, *Rev. Sci. Instrum.* **81** (2010) 073304.

[23] X. Ge et al., *A flexible, on-line magnetic spectrometer for ultra-intense laser produced fast electron measurement*, *Nucl. Instrum. Meth.* **A 887** (2018) 54.

[24] B.B. Pollock et al., *Two-screen method for determining electron beam energy and deflection from laser wakefield acceleration*, in *Proceedings of PAC09*, Vancouver, BC, Canada, pp. 3035–3037 (2009).

[25] C.E. Clayton et al., *Self-Guided Laser Wakefield Acceleration beyond* 1 *GeV Using Ionization-Induced Injection*, *Phys. Rev. Lett.* **105** (2010) 105003.

[26] H.J. Cha et al., *Absolute energy calibration for relativistic electron beams with pointing instability from a laser-plasma accelerator*, *Rev. Sci. Instrum.* **83** (2012) 063301.

[27] J.G. Gallacher et al., *A method of determining narrow energy spread electron beams from a laser plasma wakefield accelerator using undulator radiation*, *Phys. Plasmas* **16** (2009) 093102.

[28] D. Hazra, S. Mishra, A. Moorti and J.A. Chakera, *Electron radiography with different beam parameters using laser plasma accelerator*, *Phys. Rev. Accel. Beams* **22** (2019) 074701.

[29] GEANT4 collaboration, *GEANT4: A Simulation toolkit*, *Nucl. Instrum. Meth.* **A 506** (2003) 250.

[30] J. Allison et al., *Recent developments in Geant4*, *Nucl. Instrum. Meth.* **A 835** (2016) 186.

[31] S.H. Kim and C. Doose, *Temperature Compensation Of NdFeB Permanent Magnets*, in *Proceedings of the 1997 Particle Accelerator Conference*, Vancouver, BC, Canada, 16 May 1997 [DOI].

[32] A.A. Soloviev et al., *Two-screen single-shot electron spectrometer for laser wakefield accelerated electron beams*, *Rev. Sci. Instrum.* **82** (2011) 043304.

[33] Y. Lin and D.C. Joy, *A new examination of secondary electron yield data*, *Surf. Interface Anal.* **37** (2005) 895.

[34] Y.C. Wu, B. Zhu, K.G. Dong, Y.H. Yan and Y.Q. Gu, *Note: Absolute calibration of two DRZ phosphor screens using ultrashort electron bunch*, *Rev. Sci. Instrum.* **83** (2012) 026101.

[35] L.H. Brixner, *New X-ray phosphors*, *Mater. Chem. Phys.* **16** (1987) 253.

[36] T. Kurz et al., *Calibration and cross-laboratory implementation of scintillating screens for electron bunch charge determination*, *Rev. Sci. Instrum.* **89** (2018) 093303.

2020 JINST 15 P01034